Side surface topography generation during laser powder bed fusion of AlSi10Mg

E. Masiagutova, Frédéric Cabanettes, Alexey Sova, M. Cici, G. Bidron, Philippe Bertrand

Version of Record: https://www.sciencedirect.com/science/article/pii/S2214860421003900
Manuscript_b4af9e27515a9218a8655adaaadf6f45

Side Surface Topography Generation during Laser Powder Bed Fusion of AlSi10Mg

E. Masiagutova[a1], *F. Cabanettes*[a], *A. Sova*[a], *M. Cici*[a], *G. Bidron*[b], *P. Bertrand*[a]

[a]*University of Lyon, Ecole Centrale de Lyon - ENISE, Laboratoire de Tribologie et Dynamique des Systèmes, CNRS UMR 5513, 58 rue Jean Parot, 42023, Saint-Etienne, France*
[b]*Manutech USD, 20 rue PR Benoit Lauras, 42000, Saint-Etienne, France*

ARTICLE INFO

Article history:

Keywords:
Surface topography
Laser powder bed fusion
Aluminum alloy
Process parameters
Roughness optimization

ABSTRACT

Additive manufacturing (AM) is a direct manufacturing process that makes it possible to fabricate "near net shape" freeform parts. Among the many metal AM techniques, laser powder bed fusion (LPBF) is the most effective at obtaining complex structures with internal cavities, such as tortuous heat exchangers or lightweight lattice structures. AM technologies have therefore attracted considerable attention, which has led to research and development in many industries. Nevertheless, the surface topographies obtained by current AM techniques are still limiting industrial implementation for parts with high requirements. In this work, surface generation during LPBF was studied and optimized. The main aims were i) to optimize both side surface roughness and material density by studying the influence of the primary process parameters and ii) to investigate the effect of process options on side surface roughness generation for optimization purposes. The roughness dispersion and process reproducibility were also monitored and evaluated. A relationship between top and side surface roughness and material density was established. As a result, both optimizations could be performed in parallel. Analysis of the process reproducibility revealed an important roughness dispersion, especially from one side to the other. Consequently, recommendations on surface measurements were proposed. Compensations and contour settings are key parameters that can help reduce the side surface roughness. Indeed, geometrical positioning of the different weld tracks is also an important issue that must be addressed to reduce surface roughness. Based on the findings of this study, it is possible to reduce the areal average roughness *Sa* from 40 to 10 µm.

1. Introduction

Currently, the demand for mechanical and thermal properties of functional parts in the aerospace industry is high. Engineers are aiming for reliability and sustainability and to create final products while reducing their weight [1]. Consequently, some widely used alloys that have a large number of applications in this industry are aluminum–silicon alloys. Among these alloys, AlSi10Mg has an excellent combination of low weight and good mechanical properties with high heat conductivity [2–8].

Economically, the aerospace industry is trying to reduce costs from design to manufacturing. This has led to the development and use of direct manufacturing processes — namely, additive technologies. Additive manufacturing (AM) makes it possible to create freeform parts close to the final product dimensions (near net shape surfaces) [1]. Therefore, in recent years, the use of AM technologies has been leading to research and development in various industries.

AM represents a group of manufacturing processes in which the final part is formed directly from a three-dimensional computer-aided design model by adding material layer by layer. This includes techniques such as vat photopolymerization, material extrusion, material jetting, binder jetting, powder bed fusion (PBF), direct energy deposition, electron beam melting (EBM), and sheet lamination [7–9]. They are classified by the source of energy (laser, electron beam), the method of joining material (heated nozzle, binder, etc.), the group of the processed material (plastics, metals, ceramics, etc.), and the feedstock state (liquid, solid) [9].

Among metal AM techniques, powder bed fusion (PBF) makes it possible to obtain complex parts with high accuracy by using a small beam size and layer thickness [10, 11, 15–18]. PBF can use a laser as a source of energy to heat and melt fine metal particles in a powder bed [9–12]. In such cases, one can call the process "laser powder bed fusion" (LPBF) or selective laser melting (SLM). The combination of AlSi10Mg material (interesting for the aeronautic industry) with the LPBF process can lead to new opportunities, such as applications that require complex structures and internal cavities, such as tortuous heat exchangers or lightweight lattice structures [14].

[1] Corresponding authors.
E-mail address: elina.masiagutova@gmail.com (E. Masiagutova)

Nomenclature

Process parameters

P	Laser power [W]
V	Laser scan speed [mm/s]
d	Layer thickness [µm]
h	Hatch distance [µm]
LED	Linear energy density [J/mm]
VED	Volumetric energy density [J/mm^3]

Statistic parameter

σ	Standard deviation [µm]

Density parameters

$\rho_{absolute}$	Absolute sample density [g/cm^3]
$\rho_{relative}$	Relative sample density [g/cm^3]
$\rho_{theoretical}$	Theoretical density [g/cm^3]
ρ_{water}	Water density [g/cm^3]
m_{air}	Sample weight in air [g]
m_{water}	Sample weight in water [g]

Roughness parameters

Ra	Arithmetic mean height [µm]
Sa	Areal arithmetic mean height [µm]

As mentioned before, LPBF uses a laser source to melt the powder material and, as a result, form three-dimensional parts. Because the part is built up into layers, this action is performed layer by layer. A laser, in a predetermined area, forms weld tracks on a layer of metal powder (*d*) using process parameters, such as power (*P*), scan speed (*V*), and hatch distance (*h)* (see Fig. 3). The sequential combination of these weld tracks, which solidify as it cools, creates the required volumes and surfaces. The platform then lowers, and the roller deposits a new layer of powder. Thus, each area is manufactured, generating a three-dimensional part. This method of creating an object leads to the formation of two completely different surfaces:

- Top surfaces, formed by a combination of laser tracks from the last layer; and
- Side surfaces, formed by a combination of beginning and end tracks from all layers.

To date, the obtained surface roughness (top surface *Ra*: 8 to 20 µm, side surface *Ra*: 15 to 35 µm, [15, 17, 18]) is rather high compared with conventional manufacturing processes. According to the literature, simultaneously achieving a minimum *Ra* for the top and side surfaces is difficult. Indeed, different mechanisms are responsible for top and side surface generation [15, 25, 29, 30].

Therefore, the surface topographies obtained by AM techniques still limit the industrial implementation of parts with high requirements (high precision, long fatigue life, etc.) [15, 16–19]. The functionality of the produced parts can be improved by using different postprocessing technologies. These technologies increase time and production costs [2, 15]. Furthermore, it is not always possible to apply treatments that reduce surface roughness. Indeed, access to the external (lattice structures) and internal (channels) surfaces generated can sometimes be limited. Finishing is therefore not always possible, and the surfaces can remain as-built from AM, causing the part functionality to deteriorate [15]. For example, in the case of heat transfer in parts with small tortuous cooling channels, the pressure drop depends strongly on the side surface roughness [15, 16].

Consequently, it is important to study and improve the AM as-built surfaces. A better understanding of the LPBF process and the surface generation at the laser track and workpiece scale can help to reduce the roughness of AM parts.

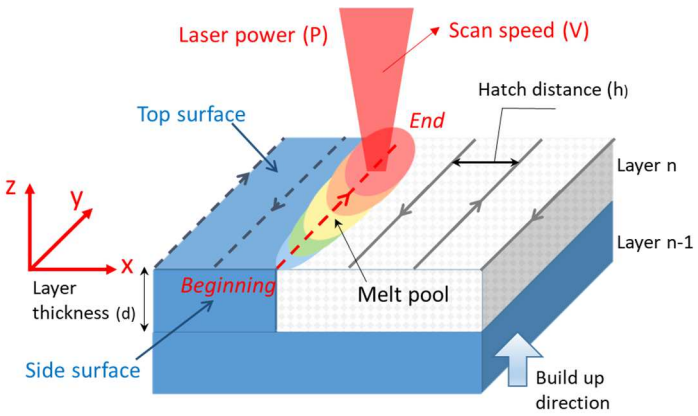

Fig. 3. Volume formation in LPBF process and corresponding surfaces generated

Fig. 4 presents an overview of the strategy to improve the functionality of parts. Different process factors are responsible for different undesired physical phenomena appearing during LPBF. The physical phenomena directly influence part functionality, such as part density or roughness. To reduce the roughness of as-built surfaces, it is necessary to understand the role of a large number of interrelated process factors and their associated physical phenomena.

The process factors can be classified into three major families:

- Powder properties
- Process parameters
- Workpiece configuration

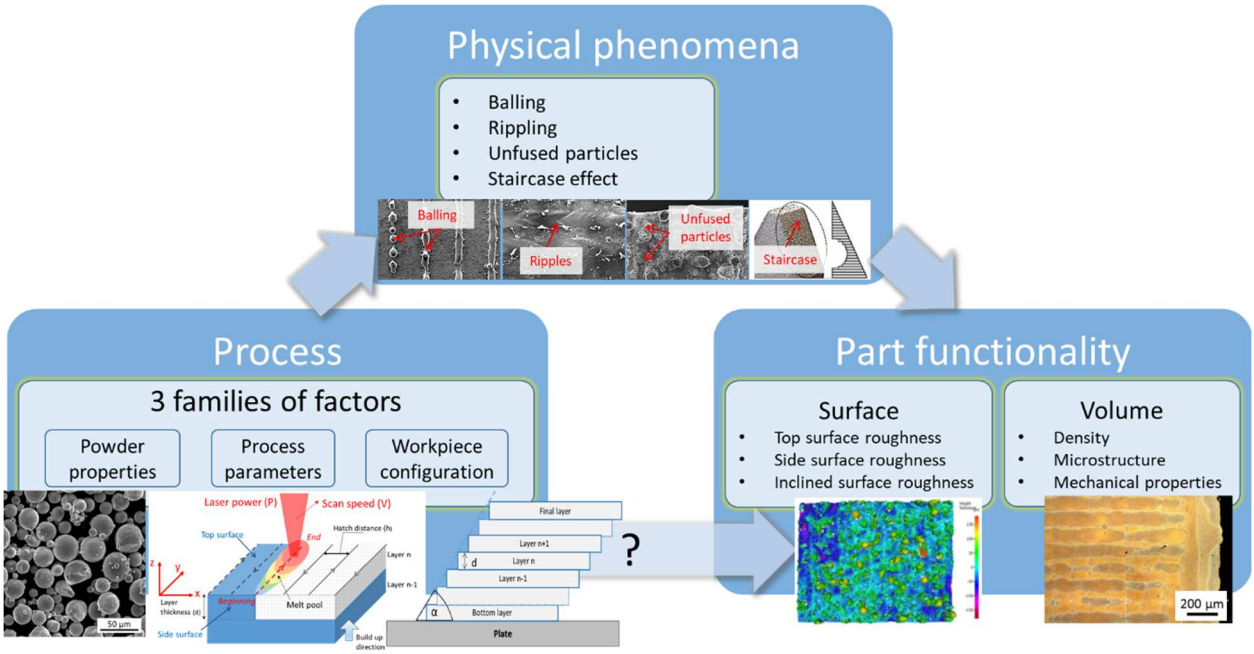

Fig. 4. Relationship between process, physical phenomena, and part functionality

Concerning undesired physical phenomena, the most common ones appearing during LPBF are listed below.

- Balling is a phenomenon in which molten metal forms spheroidal balls owing to insufficient wetting of the previous layer and insufficient surface tension [22, 26–28, 37]. It prevents the generation of continuous melt tracks and forms rough and bead-shaped surfaces.
- The rippling effect can influence the roughness of the top surface. This occurs when surface tension exerts important shear forces on the liquid surface [25].
- The presence of unfused and attracted particles on the side surfaces is shown in Fig. 5. The high temperature of the melt pool tends to cause more partially melted powder to attach to the solid interface [18, 36].
- The build orientation intrinsically generates a staircase effect. This depends on the inclination angle and

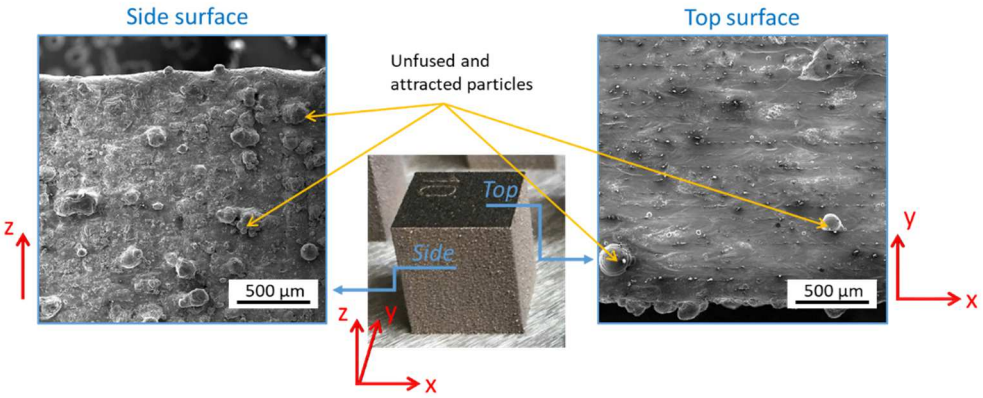

layer thickness. This is inherent to any layer-manufacturing technique [18, 21, 26, 32, 33].

Fig. 5. Surface roughness that has deteriorated because of the presence of unfused particles on AM samples

The link between process parameters, undesired physical phenomena, and functionality is rather complex, and several studies have addressed some of these issues. Table 2, shows a review of the literature and the links treated by each article. The two columns on the left part of Table 2 show the process factors and associated physical phenomena. In the right part, the potential effects of these phenomena on top/side roughness and density are listed, and references are classified according to their conclusions ("Yes" if the article mentions a link with the physical phenomena and "No mention" otherwise). It is worth noting that there are other works that have not been included in Table 2.

Table 2.
Review of process factors, their influence on physical phenomena, and potential consequences for part functionality

	Process factors and parameters	Undesired physical phenomena generated	Potential effect on side roughness	Potential effect on top roughness	Potential effect on density	References
AlSi10MG powder properties	Absorptivity, Reflectivity, and oxidation	Balling effect	Yes	Yes	No mention	[26]
			No mention	No mention	Yes	[27, 28, 37]
	Thermal conductivity, Cooling, and heat dissipation rates	Rippling effect	No mention	Yes	No mention	[25]
Process parameters	Linear energy density P/V	Balling, rippling, unfused and attracted particles	No mention	Yes	Yes	[6, 8, 31, 37, 38]
			Yes	Yes	No mention	[25, 30, 35, 36, 39]
			Yes	No mention	No mention	[29, 31]
			No mention	No mention	Yes	[14, 27]
			No mention	Yes	No mention	[17]
	Layer thickness	Staircase effect	Yes	No mention	No mention	[18, 32, 33]
	Hatch distance	Attracted particles	Yes	Yes	No mention	[36]
			Yes	No mention	No mention	[18, 39]
			No mention	No mention	Yes	[8]
Work piece	Build orientation	Staircase effect	Yes	No mention	No mention	[18, 21, 26, 32, 40, 45, 46]

This table demonstrates that the part density and surface roughness have rarely been studied simultaneously. Furthermore, when studied, the side surface roughness generation is mainly understood geometrically (layer thickness, hatch distance, and build orientation).

1.1. Aim of the study

As explained above, many studies have focused on the influence of process parameters on the densification, microstructure, and mechanical properties of the final parts [11–14, 17, 27, 28]. Top-surface topography has also been investigated [2, 6, 8, 17, 30, 31]. Only a few studies have simultaneously studied the density and side surface roughness of the parts [32, 36, 39]. In addition, few articles have emphasized the factors and physical phenomena that influence the side surface roughness [25, 33, 35]. Most research on improving the quality of the side surface is limited to postprocessing, such as machining or polishing [2, 36].

Consequently, the mechanisms of side surface generation in the LPBF process are still poorly understood. In addition, side surface roughness is rarely optimized while considering part density optimization. Finally, surface topography dispersions caused by the process are often disregarded, making correlation analysis more difficult.

Therefore, in this article, the study of side surface generation and its optimization is proposed in three stages.

- First, the LPBF process is optimized by finding an optimal parameter window for AlSi10Mg. This will allows finding a part density optimum for a reasonable first roughness optimum (primary parameter optimization).
- The surface roughness dispersion resulting from the process is analyzed, including the process reproducibility over different building plates, process reproducibility over the same building plate, surface roughness dispersion on a workpiece, and surface roughness dispersion on a single workpiece face (surface roughness dispersion study). Based on this analysis, surface acquisition recommendations are proposed and applied to the rest of the study.
- Finally, the effects of different process options (contour and compensation) are studied to better understand side surface generation and optimize it (secondary parameter optimization).

2. Experimental conditions and methods

2.1. Material and equipment

In this study, gas-atomized AlSi10Mg (composition shown in Table 3) powder produced by TLS Technik[2] was used. The powder had a spherical shape (see Fig. 6), and its size distribution (see Fig. 7) ranged from 5 to 25 µm. Before sample fabrication, the powder was dried at 100 °C for 1 h to reduce the humidity and the residual oxygen content of the powder [8, 27].

Table 3.
AlSi10Mg chemical composition in weight % (TLS Technik)

Al	Si	Mg	Fe	Cu	Zn	Mn	Other
Balance	9–11	0.2–0.45	≤0.55	≤0.05	≤0.1	≤0.45	≤0.05

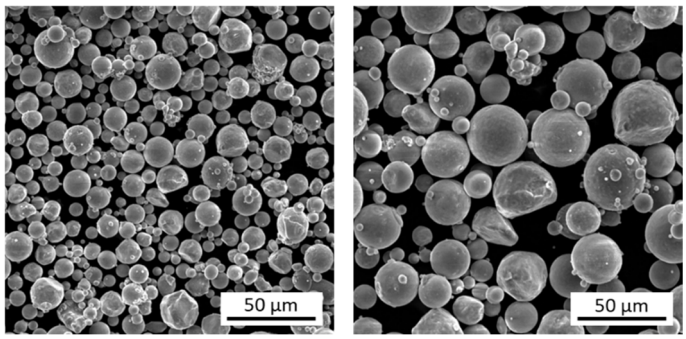

Fig. 6. SEM image of AlSi10Mg powder used for this study

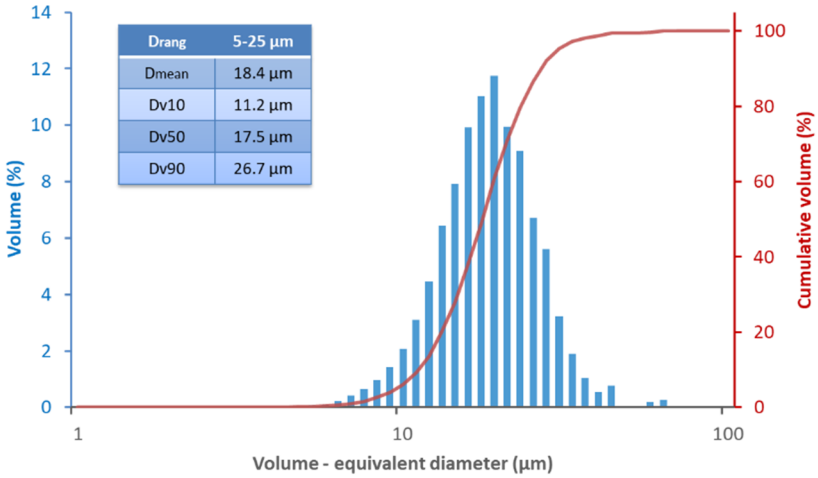

Fig. 7. AlSi10Mg powder size distribution

[2] TLS Technik GmbH, Germany. http://www.tls-technik.de

Samples were produced using a ProX DMP 200[3] LPBF machine (technical specifications are presented in Table 4). The process was carried out in a chamber under an inert atmosphere (argon). The powder distribution and gas direction are shown in Fig. 8.

Table 4.
Main technical specifications of the ProX DMP 200 LPBF machine

Parameters	Values
Laser wavelength (nm)	1070
Max laser power, P (W)	400
Laser beam size (in focus, µm)	70
Laser scanning speed range, V (mm/s)	30–2000
Building envelope (mm)	140 × 140 × 100
Layer thickness range, d (µm)	10–50

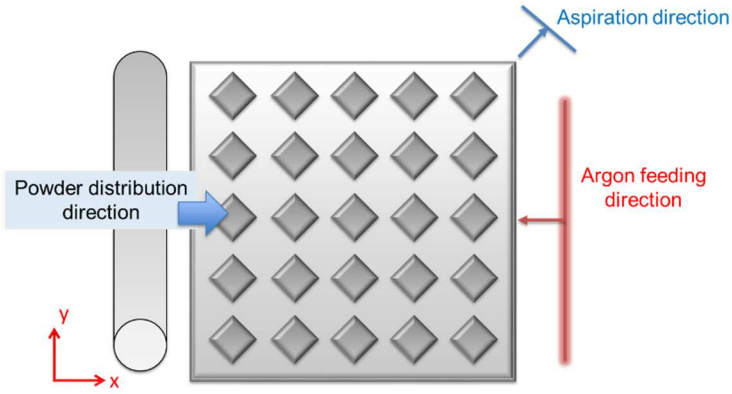

Fig. 8. Top view of the built platform showing powder distribution, gas directions, and samples layout

2.2. *Experimental procedure and variables*

Fig. 9 is a key figure to understand the global approach of this work. It summarizes the different experimental sequences of this study.

- Two process optimization steps are performed: i) primary parameter optimization to find the first parameter window (optimum part density and first reasonable roughness optimum) and ii) secondary parameter adjustments (contour and compensation) to better understand the side surface generation and optimize its roughness.
- A study on roughness dispersion resulting from the process is performed after the first optimization, and surface characterization recommendations are obtained and applied for the rest of the study.

Primary parameter optimization: Basic parameters of the LPBF process, such as laser power (P in W), scan speed (V in mm/s), hatch distance (h, µm), and layer thickness (d, µm)), are first optimized. The optimization is carried out in two stages.

The shape of the first weld tracks was optimized by varying the laser power and speed: linear energy density (LED) optimization. The LED (in J/mm) is defined as the ratio of laser power to scanning speed (see Eq. (1)) and is commonly used for this first-step optimization.

$$LED = \frac{P}{V} \tag{1}$$

[3] 3D Systems, USA. http://www.3dsystems.com

Second, based on the laser power and speed optimal window found, a volumetric optimization is performed: a volumetric energy density (VED, in J/mm²) parameter is defined and serves as a unique parameter to optimize the built volumes. The VED is calculated according to Eq. (2). A wide range of scan speeds, laser powers, and hatch distance can be examined and gathered under the unique VED parameter. Then, the parameter window with the optimal roughness and density values can be set.

$$VED = \frac{LED}{h \cdot d} = \frac{P}{V \cdot h \cdot d} \tag{2}$$

Surface roughness dispersion study: After the first optimization, a surface roughness dispersion study is performed to evaluate the process reproducibility. For the given optimal set of primary parameters found, the process reproducibility in terms of surface roughness is evaluated for different plates (same sample arrangement) and also for one plate but on different sample positions. The roughness dispersion is also examined on different sides of one sample and for different surfaces of one side (see Fig. 9). This intermediate study makes it possible to determine whether surface roughness improvements due to a parameter are significant.

Secondary parameter adjustments: optimal primary parameters are selected and used for this second sequence. Two types of secondary parameter (or process option) are studied: compensation and contour parameters. These parameters are defined in more detail in the path followed by the laser. More explanations are given in Sections 3.3.1 and 3.3.2.

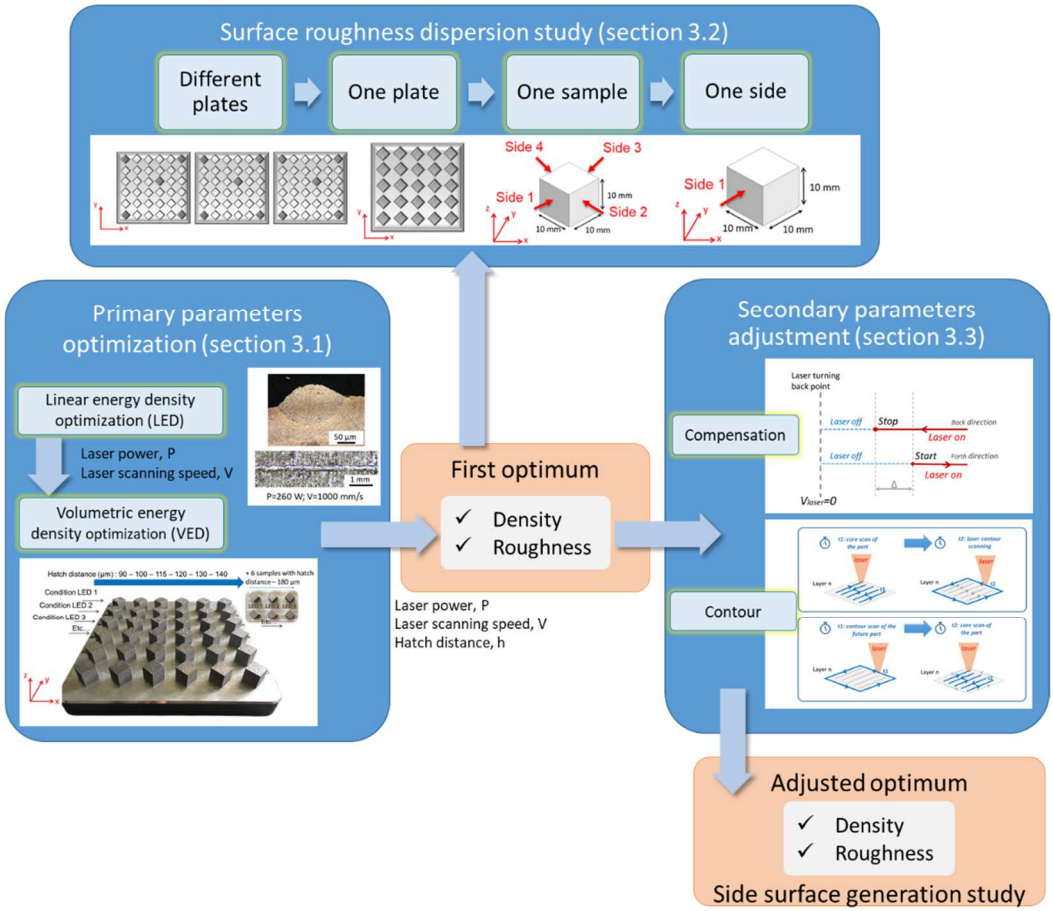

Fig. 9. Schematic representation of the process optimization stages selected for this study

2.3. Fixed parameters and configurations

It was decided that the layer thickness, spot diameter, and focalization were fixed (see Table 5) and did not change throughout the experimental procedure. These values correspond to the manufacturer's recommendations.

Table 5.
Fixed parameters

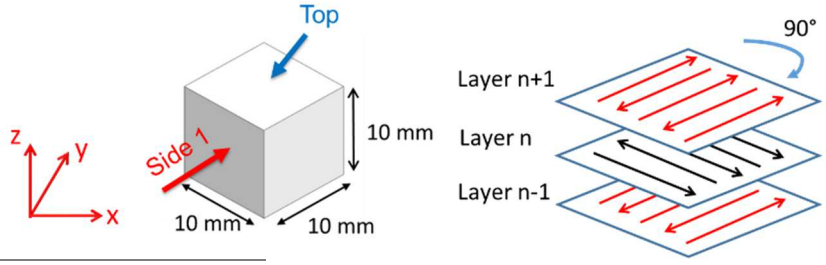

Parameters	Values
Spot diameter (µm)	70
Focalization (º)	0
Layer thickness, d (µm)	30

Furthermore, the test samples were made with dimensions of 10 × 10 × 10 mm. Each layer was scanned with back and forth tracks, and the scan direction was shifted by 90° from one layer to the other. Side 1 and the top side (see Fig. 10) were always chosen as the reference sides for measuring the roughness values.

Fig. 10. Left: test sample with Side 1 and top surfaces selected to measure the values of surface roughness; right: scan strategy with back and forth tracks shifted by 90° from one layer to the other

2.4. Sample characterization

To observe the topographies and material density, the following characterization methods were used:

Archimedes' method was used for determining the relative density of the samples. The instrument used was an analytical balance AB104-S/Fact[4]. In this experiment, the sample was weighed in air (m_{air}, g) and then in distilled water (m_{water}, g) with a known density (ρ_{water}, g/cm^3). The absolute density ($\rho_{absolute}$, g/cm^3) was calculated as follows:

$$\rho_{absolute} = \frac{m_{air}}{(m_{air} - m_{water})} \cdot \rho_{water} \quad (3)$$

Then, the relative density ($\rho_{relative}$, g/cm^3) can be determined as the ratio of the absolute density ($\rho_{absolut}$, g/cm^3) to the theoretical density ($\rho_{theoretical}$, g/cm^3):

$$\rho_{relative}(\%) = \frac{\rho_{absolut}}{\rho_{theoretical}} \cdot 100 \quad (4)$$

where $\rho_{theoretical} = 2.67$ g/cm^3 for the aluminum alloy. The porosity level can then be computed, and it corresponds to Equation (5):

$$Porosity(\%) = 100 - \rho_{relative}(\%) \quad (5)$$

Optical microscopy (ZEISS Axioscope A1) was used to determine the porosity of the sample cross section (2D surface). Cross-sectional images were obtained in the XY and YZ planes at magnifications of 5 and 10 times. The Z direction indicates the building direction (see Fig 10). Then, porosity detection was performed and the percentage was obtained by image analysis in MATLAB R2018b (version 9.5)[5].

Focus variation microscopy (Infinitefocus G5[6]) was used to acquire top and side surface topographies with lateral and vertical resolutions of respectively 2 µm and 50 nm (software settings). A magnification of 20X was used and the area measured for each sample was 3 × 2 mm corresponding to 4 × 3 stitched single surfaces with an overlap of 6%. A form removal filter (polynom of order 2) was applied to the acquired topographies. No further filters were used. The areal average roughness *Sa* (µm) parameter was used to characterize the as-built surfaces.

Scanning electron microscopy (SEM, TESCAN Vega II SBH[7]) was used for qualitative surface observations with a measured size of 2.02 × 2.02 mm.

3. Results and discussion

The general approach of this work is summarized in Fig. 9. Section 3.1 is focusing on primary parameter optimization to find the first parameter window (optimum part density and first reasonable roughness optimum).

[4] Mettler Toledo, Switzerland. https://www.mt.com
[5] MATLAB, France. https://www.mathworks.com
[6] Alicona Imaging GmbH, Austria. http://www.alicona.com
[7] TESCAN, Czech Republic. http://www.tescan.com

Section 3.2 is focusing on roughness dispersion resulting from the process first optimization. Section 3.3 is focusing on secondary parameter optimizations (contour and compensation).

3.1. Primary parameter optimization

Achieving the best surface roughness can be somewhat challenging during the laser melting process because it is an interrelated process that can harm other properties, such as porosity, at the same time. However, part density (and, thus, porosity level) is one of the most important properties to optimize because it has a direct influence on the part's mechanical and physical performance [14, 31]. Therefore, it is necessary to establish a relationship between porosity and roughness and to choose the correct process window that is optimal for both features.

LED optimization: Twenty-four single tracks were produced with different power and scan speed values (see Table 6). These tracks were made on a support to obtain a homogeneous distribution of the powder layer (the premier layers of powder adhere to the plate and, therefore, are not always homogeneous). Single weld tracks were evaluated both by top-view observations (to check the weld track continuity) and cross-section observations (to check weld track depth and height).

Fig. 11 shows the influence of different LED values on the shape of the single tracks observed by cross sections. The right side of the figure represents the weld tracks produced with a high LED (high power and low scanning speed). As observed, a LED that is too high increases the volume of the molten pool and decreases the viscosity owing to the longer duration between the laser beam and materials [8]. In this case, the melt hydrodynamics become more important (the Marangoni effect), leading to distortion and irregularity, as mentioned by Pei et al [8] and Kempen et al [14]. In addition, the cross section of the single tracks shows a very deep penetration into the previous layers. Partial evaporation can occur at high LED values [8, 14, 18]. Consequently, excessive energy tends to produce irregular and distorted weld tracks [30].

However, too low an LED (low power and high scanning speed) tends to generate droplets and a balling effect (left side of Fig. 11). Increasing the scan speed increases the width of the molten pool while its length decreases [8, 14, 30]. The elongated molten pool becomes unstable and then splits into balls to attain an equilibrium shape (Plateau–Rayleigh instability) [14]. In addition, the material absorbs less energy, and low wetting with the substrate may occur, creating droplets. Finally, the cross sections show an insufficient connection of the weld track with the previous layer [14].

As a consequence, based on top view and cross-section weld track observations, an optimal process window was chosen in the range of 0.26 to 0.33 J/mm (middle of Fig. 11). At such a level, regular and stable weld tracks were obtained. This window differed from the values reported in the literature (in the range of 0.15–0.25 J/mm) [14]. However, these results were obtained for different powder size distributions (15–45 µm). Therefore, obtaining a higher range of LED, in our study, may be due to the fact that a finer powder is used. Indeed, fine powders are more affected by the cohesive force and has poor flowability [41, 42]. Poor flowability does not allow the creation of a uniform powder layer of constant thickness [41]. This creates uneven absorption of the laser beam in the melting zone [12, 41, 42]. As a consequence, higher energies would be required for smaller powders.

Table 6.

Primary process parameters selected for LED optimization

Parameters	Values
Laser power, P (W)	200, 220, 240, 260, 280, 300

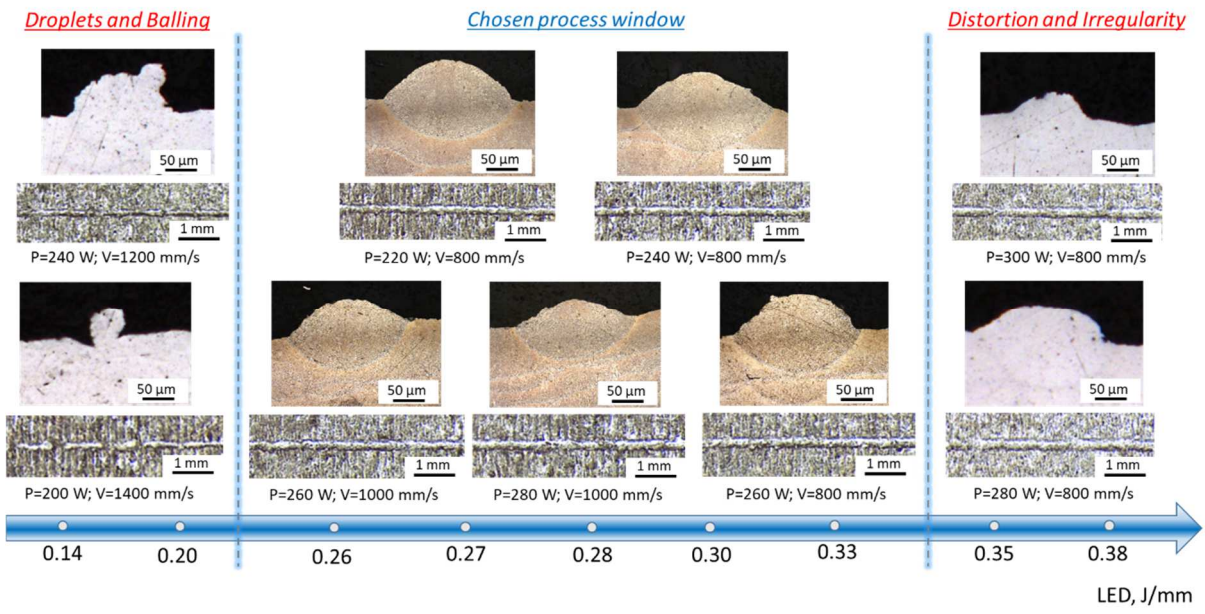

Scan speed, V (mm/s)	800, 1000, 1200, 1400

Fig. 11. Cross sections of single weld tracks with different LED values

VED optimization: In combination with the LED process window, several hatch distances (see Table 7) were selected, and the VED (defined in Section 2.2) was computed. The principal LED values were chosen within the optimal parameter window. Forty-two samples with different VEDs were built (see Fig. 12). In addition, four samples outside the optimal LED window were produced to confirm the LED optimization findings. As mentioned in Section 2.3, the layer thickness was constant and equal to 30 µm.

Table 7.
Primary process parameters for VED optimization

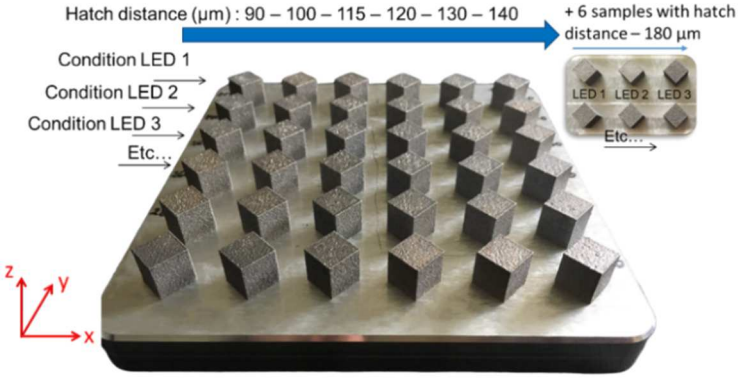

Parameters	Values	Power, P (W)	Scan speed, V (mm/s)	Hatch distance, h (µm)
LED 1 (J/mm)	0.26	260	1000	90, 100, 115, 120, 130, 140, and 180
LED 2 (J/mm)	0.27	220	800	
LED 3 (J/mm)	0.28	280	1000	
LED 4 (J/mm)	0.30	240	800	
LED 5 (J/mm)	0.30	300	1000	
LED 6 (J/mm)	0.33	260	800	

Fig. 12. Samples with selected LED parameters and varying hatch distances

The samples obtained in Fig. 12 can be subjected to roughness variations because of the different locations on the plate (caused by laser caustic instabilities and gas flows). The study of homogeneity on one plate is therefore an important step, and it is discussed in Section 3.2. Nevertheless, the trends discussed in this section relating surface roughness to VED are significant.

The main effects of the VED on the top and side surface roughnesses and porosity levels are shown in Fig. 13. According to this figure, the porosity and areal average roughness *Sa* (for the top and side surfaces) exhibit similar trends. Indeed, three distinct behaviors can be observed.

- For low VED values, the surface roughness and porosity level decreased with an increase in VED.
- Then, as the VED continued to increase, the surface roughness and porosity reached an optimum (minimum value).
- Finally, for high VED values, an increase in VED leads to an increase in the roughness and porosity level.

These trends can be explained as follows. Low VED values generate partial melting of the powder. Consequently, high porosity and roughness levels were obtained. Higher energy increases the size of the melted area, allowing better melting of powder beds and enhanced wettability with previous layers [23, 35, 38]. This promotes surface smoothing and porosity-level reduction [23]. However, an excessively high energy generates high temperature gradients in the melt pool, and the created sample surface becomes warmer, attracting sintered particles

[26, 35]. The surfaces become irregular with a large number of attached powder particles, but the level of porosity changes slightly [35].

This observation is corroborated by Fig. 13, where three samples with different VED values (27.8, 61.9, and 100 J/mm^3) were observed by SEM (bottom of Fig. 13). Samples 1 and 3 had a poor surface quality. For the first sample, there was not enough energy for overlapping gaps between the weld tracks and to melt the powder layer completely. In addition, unmelted particles stuck to the surface owing to partial remelting. For the third sample, the surfaces became irregular because of the presence of a large number of bowls (molten and solidified material) partially integrated into the surface. The balling phenomenon propagated at higher energy because of the large difference in surface tension generated around the melted particles (caused by high temperature gradients) [26].

To conclude, the optimal window of volumetric energy densities (minimum average surface roughness and minimum porosity level) ranges from 60 to 85 J/mm^3. In this optimal window, the average roughness *Sa* reaches 20 µm, and the density reaches 99.6% (0.4% porosity). The optimal conditions (P = 260 W, V = 1000 mm/s, and h = 140 µm) with VED of 61.9 J/mm^3 were chosen as the basis for the rest of the study.

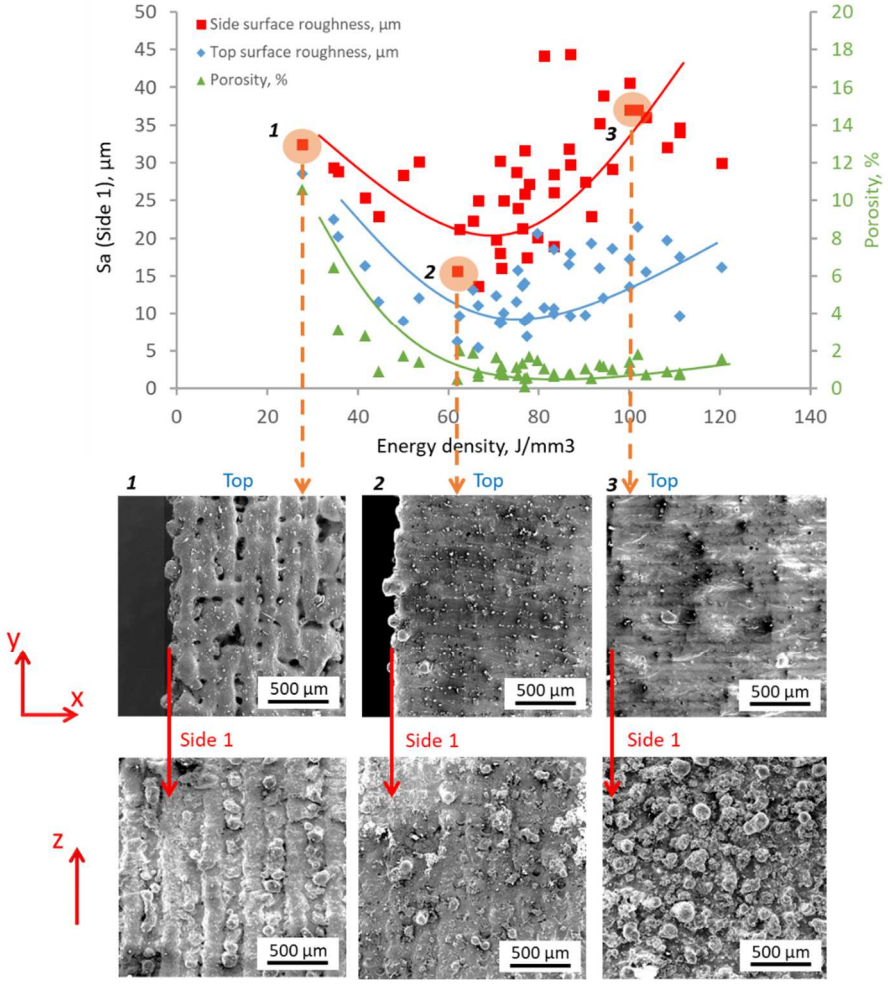

Fig. 13. Surface roughness and part density as a function of volumetric energy density (VED)

3.2. *Surface roughness dispersion study*

Before the secondary parameter optimization, it is necessary to evaluate the roughness dispersions obtained by the process. This study was performed for the samples produced under the aforementioned optimal conditions (laser power: 260 W, scanning speed: 1000 mm/s, hatch spacing: 140 µm, leading to VED = 61.9 J/mm^3). Roughness variations may be caused by the following:

- Production from different plates
- Different locations of samples on the same plate
- Different sides of the sample characterized
- Location of the measured surface on one side of the sample

Fig. 14 shows the four different types of variation that were studied separately. In this study, the definition of "roughness reproducibility" is used for samples produced on different plates or on one plate and "roughness dispersion" for the surfaces produced on one sample or on one side of the sample. As indicated above, for this study, samples were repeatedly produced with the same procedure and process conditions. Furthermore, sample side 1 was always selected to measure roughness.

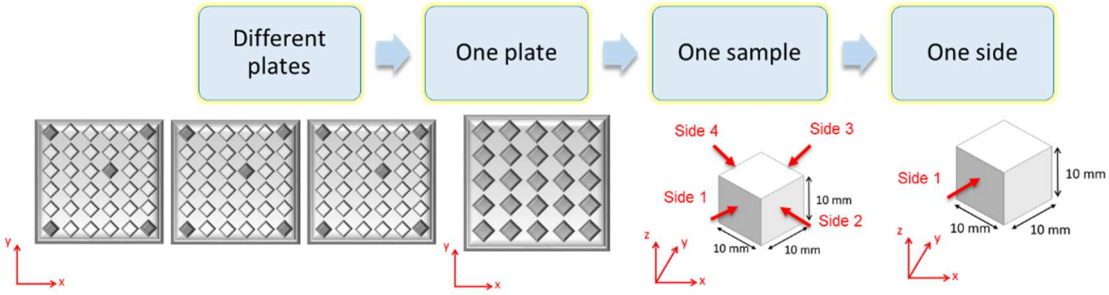

Fig. 14. Surface roughness dispersion study from plates to sample and from sample to side

Roughness reproducibility for different plates: First, three plates were manufactured to check the surface reproducibility on different plates. On each of these plates, among the different samples, five were produced with the same parameters and placed at specific locations: (see Fig. 15): i) sample 1, bottom left corner; ii) sample 2, bottom right corner; iii) sample 3, center; iv) sample 4, top left corner; and v) sample 5, upper right corner.

The bottom left part of Fig. 15 shows that the average values of roughness vary in the range of 24.1 to 22.2 µm from plate to plate. In this graphic, error bars represent the measured standard deviation for plates 1–3, respectively ($\sigma = 3.75, \sigma = 2.05,$ and $\sigma = 1.07$ µm). The roughness variations from one plate to the other seem to be rather low. However, the surface roughness varies greatly depending on the location on the plate (bottom right part of Fig. 15). The roughness values are rather high in the corners of the plates and seem to be lower and more stable in the middle of the plates. This may be because of the powder bed thickness inhomogeneity [41] and gas flow and aspiration directions [35].

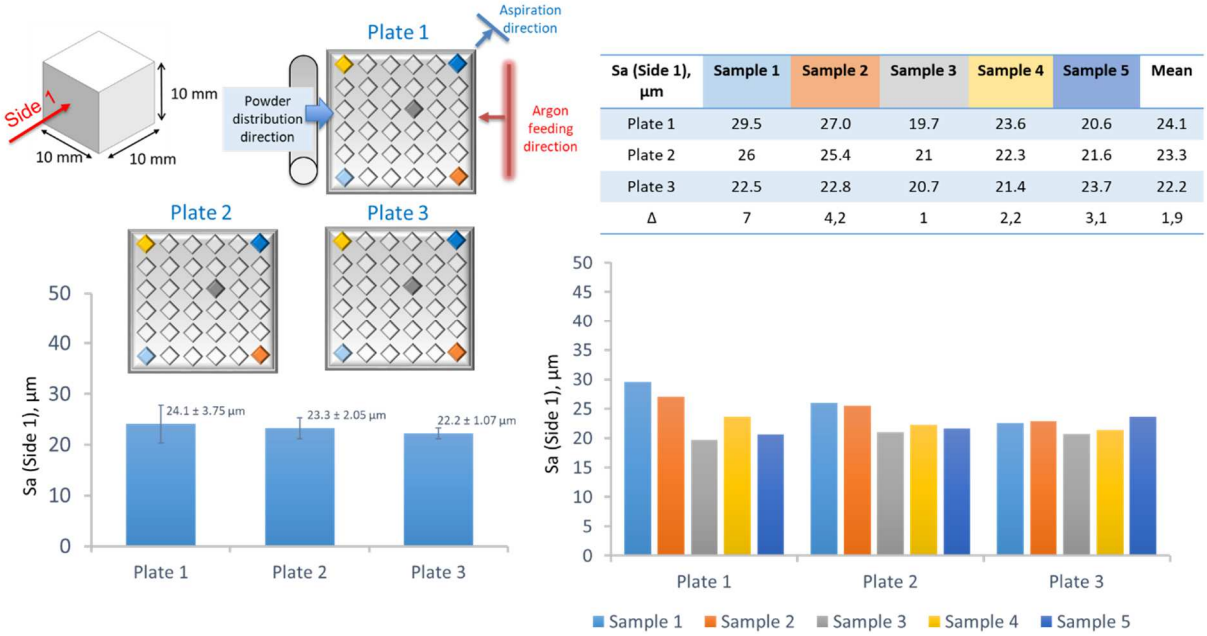

Sa (Side 1), µm	Sample 1	Sample 2	Sample 3	Sample 4	Sample 5	Mean
Plate 1	29.5	27.0	19.7	23.6	20.6	24.1
Plate 2	26	25.4	21	22.3	21.6	23.3
Plate 3	22.5	22.8	20.7	21.4	23.7	22.2
Δ	7	4,2	1	2,2	3,1	1,9

Fig. 15. Reproducibility of roughness on different plates

Roughness reproducibility for different sample locations on one plate: For this analysis, 25 samples were made at different locations on one plate for better monitoring of the roughness variations (see Fig. 16). The figure shows that the surface roughness was higher when the samples were located far from the argon feeding and

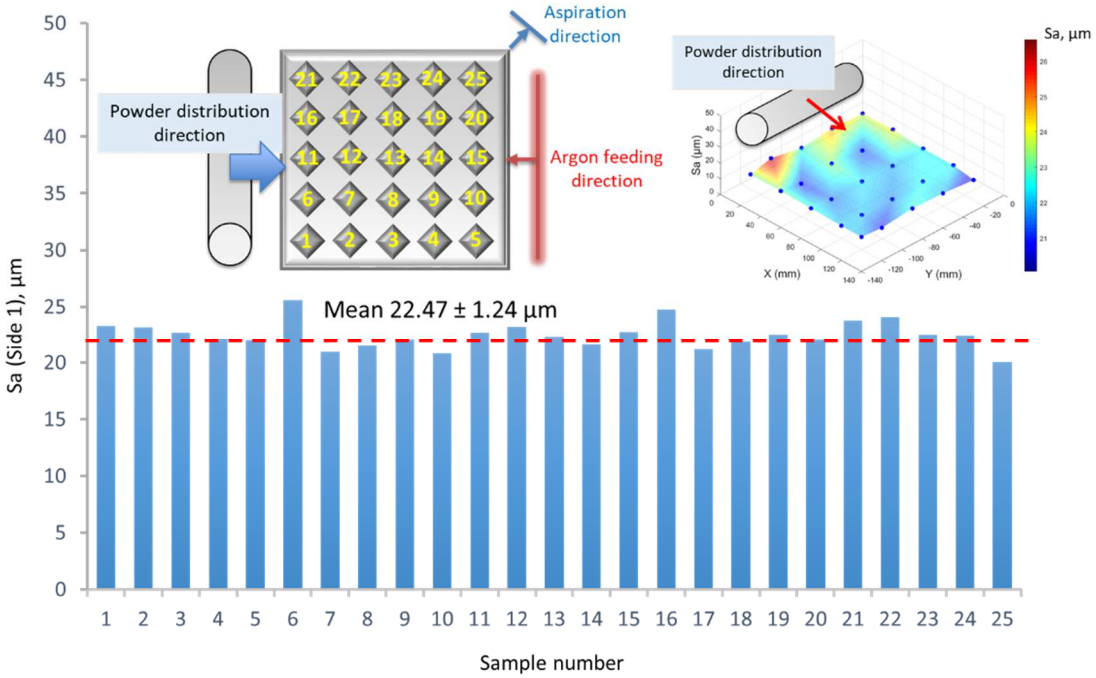

aspiration vent.

Fig. 16. Mapping of sample roughness values for different build plate locations

Therefore, this study confirms the first findings in Fig. 15. In this case, *Sa* could vary from one sample to the other, even though the same process conditions were used. This variation was characterized by a standard deviation $\sigma = 1.24$ µm. In following sections, this standard deviation value is used to plot the error bars on the graphs. The rest of the studies were performed on the same plates, so roughness variations resulting from sample location could occur.

Roughness dispersion on different sides of one sample: Considering the roughness within the same sample, it can be seen that surfaces measured on sides 1 and 2 are significantly different from those measured on sides 3 and 4 (see Fig. 17). The reason for such differences is that the size of the cubes (10 × 10 mm) is not a multiple of the hatch distance h =140 µm ($\Delta 1 \neq h < 140$ µm, and $\Delta 2 = h = 140$ µm, see Fig. 18). Consequently, for sides 1 and 2, the weld tracks that are parallel (even layers, see Fig. 18a) to the final surface of interest are hidden by weld tracks perpendicular (odd layers, Fig. 18b) to the final surface. One can see on surfaces from side 1 and 2 patterns from perpendicular weld tracks (see Fig. 18c). In contrast, for sides 3 and 4, the weld tracks that are parallel (even layers, Fig. 18a) to the final surface of interest hide the weld tracks perpendicular (odd layers, Fig 18b) to the final surface. Consequently, a better roughness is obtained (Fig. 18c). More importantly, for the rest of the study, only side 1 surfaces were evaluated, meaning that the roughness values are particularly high. Therefore, the measured side

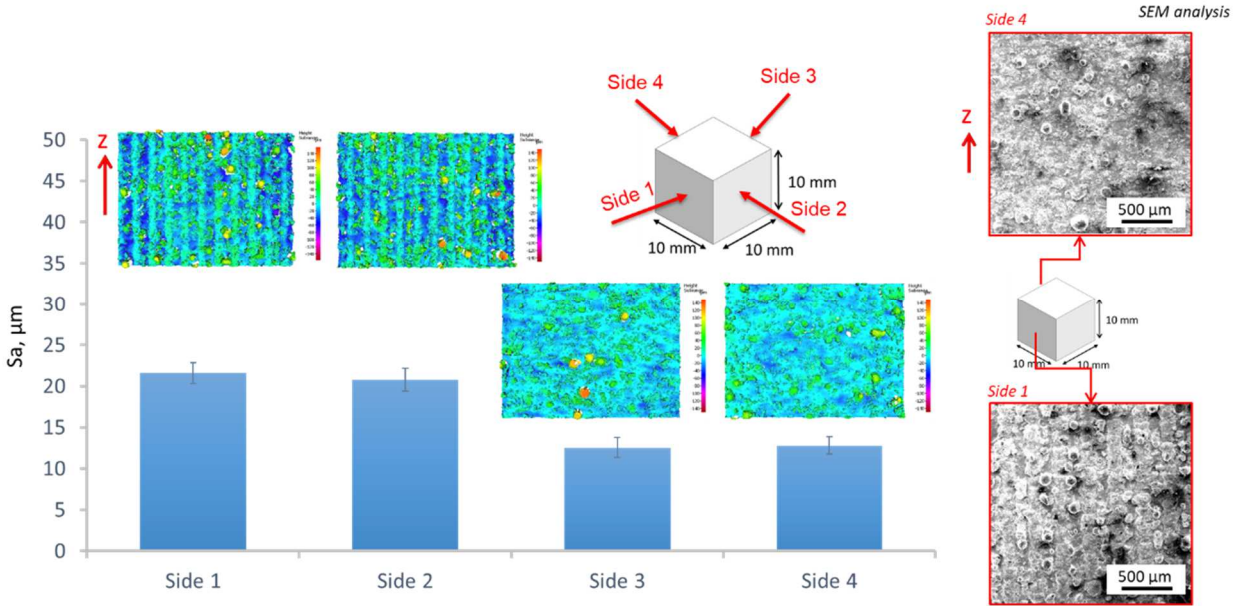

should always be mentioned to maintain consistent observations.

Fig. 17. Roughness distribution on different sides of one produced cube

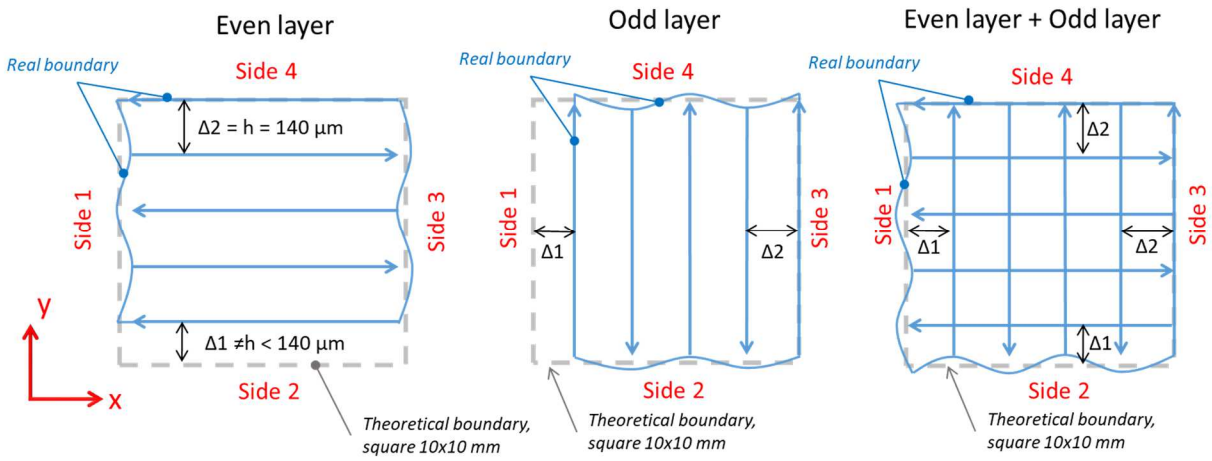

Fig. 18. Schematic representation of the formation of sides by crossing even and odd layers at a surface size of 10 × 10 mm and a hatch distance of 140 µm: a) even scan layer parallel to the final surface; b) odd scan layer perpendicular to the final surface; c) crossing even and odd scan layers

Roughness dispersion for different locations on one side of one sample: Nine surface topography measurements (size: 3 × 2 mm) were made on side 1 (total size: 10 × 10 mm), meaning that the full area of one side

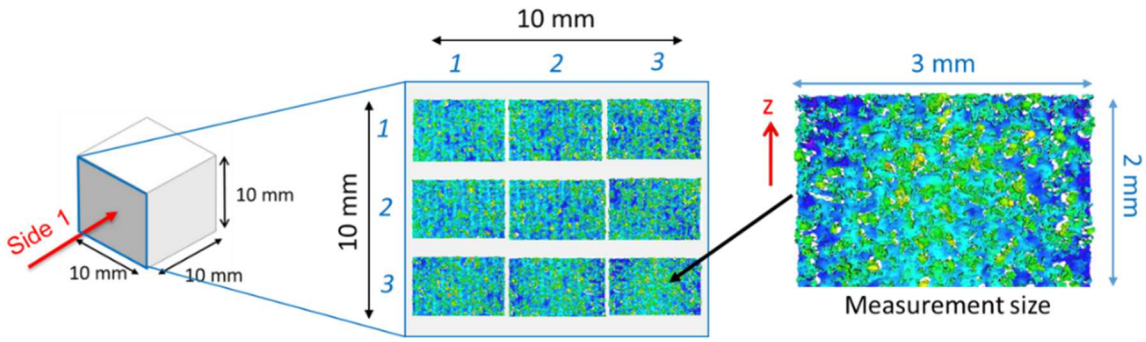

was monitored (see Fig. 19).

Fig. 19. Roughness dispersion on one side of produced cube

Nine surface measurements were performed on the other sides of the sample, and the areal average roughness *Sa* is plotted in Fig. 20. The dispersions of roughness on one side were rather low compared with dispersions from one side to the other. Furthermore, the roughness value on the central part of one side was close to the average value of the nine measurements. As a consequence, measurements were taken in the central part of side 1 for the rest of the study. This measuring strategy was already applied to the primary optimization study in Section 3.1.

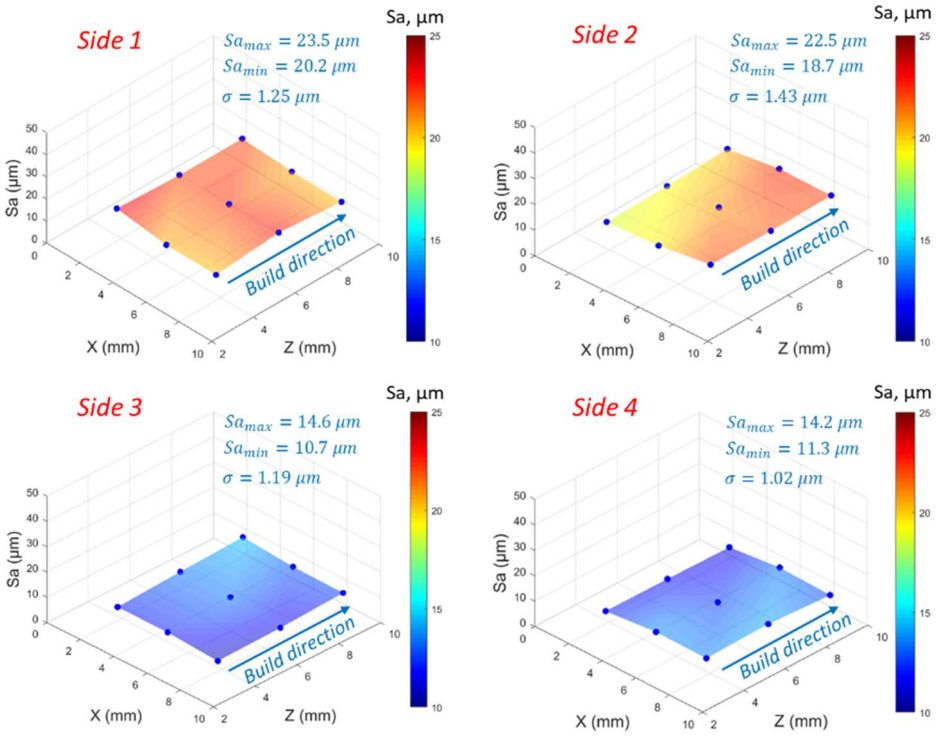

Fig. 20. Surface roughness dispersion on the four sides of a cube

Surface roughness reproducibility and dispersion summary: Important results concerning the surface roughness characterization of AM surfaces were obtained and are summarized below. Some characterization and acquisition recommendations are given.

- The roughness variations from one plate to the other can be rather low but greatly depends on the location on the plate: high in the corners of the plates (variation up to 7 µm) and much lower in the middle of the plates (variation of 1 µm).
- The average roughness *Sa* can vary with a standard deviation $\sigma = 1.24$ µm. Consequently, an error bar equal to two standard deviations is used on the areal average roughness graphs of the rest of this study.
- Differences in areal average roughness from one side to the other are significant and can reach as much as 9 µm ($\sigma = 4.9$ µm). This is because the sample size is not a multiple of the hatch distance, leading to different weld track configurations on each side. Therefore, it is recommended that the same sample side always be measured for comparison purposes.
- Finally, roughness dispersions on the same side of a sample are rather low (approximately 2 µm with $\sigma = 1.25$ µm). It is recommended at least to measure on the center part of the side to obtain a representative average roughness.

3.3. Secondary parameter adjustment

The recommendations found in Section 3.2 are applied for this study. Further roughness improvements can be achieved by adjusting the secondary process parameters. In this study, it has been found that among the wide range of secondary parameters, two clearly had some influence on roughness. They are presented below. To improve the generated roughness ($Sa \approx 20$ µm), adjustment options, such as compensation and contour, are used. The density of the samples was checked and remained stable (variation from 99.6% to 99.8%).

3.3.1. Compensation

To understand the compensation parameter, it is necessary to consider the back and forth laser paths (see Fig. 21) when turned on and turned off. First, it is important to know that, even when turned off, the laser target continues to move forward. When turned off, the laser target keeps moving so that the laser is at its nominal speed when turned on again. This can be explained by Fig. 21 as follows: when traveling in the back direction, the laser being turned on (path marked in red) is turned off at a "stop position" but continues to move (path marked in blue). It then decelerates until it reaches the turning back point (zero speed). Afterward, it is shifted by a hatch distance and then accelerates in the forth direction (path marked in blue) until it reaches a constant nominal speed at a "start position." At this moment, the laser is turned on and starts producing again (path marked in red). The compensation is, therefore, an extension of the computed trajectories, at the beginning and at the end of the scan vectors, which is necessary to produce samples with a constant laser speed. Moreover, it can also influence overheating [18]. The compensation makes it possible to change the start and stop positions. The parameter of interest in this part of the study is the difference between the start and stop positions Δ. Therefore, it is expressed in micrometers.

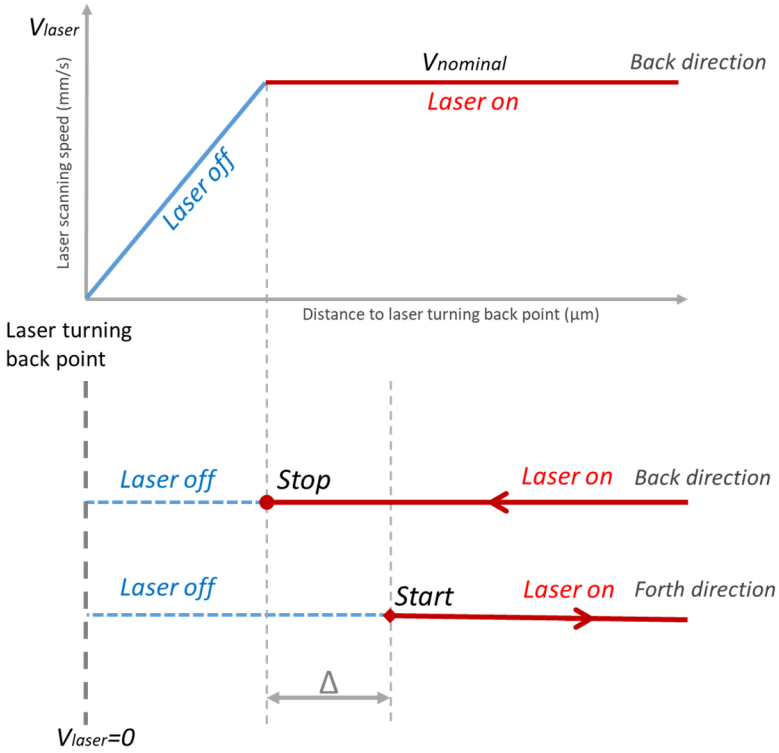

Fig. 21. Schematic representation of the laser path including compensation parameter

Delta (Δ) is defined as the difference between the start and stop points: Δ = Start–Stop. It can be positive (Δ > 0 => Start > Stop), negative (Δ < 0 => Start < Stop), or zero Δ = 0 => Start = Stop (see Fig. 22). In this experiment, the tart position was kept constant, and the end position was changed. Here, Δ varied from −140 to 140 µm in steps of 20 µm (see Table 8).

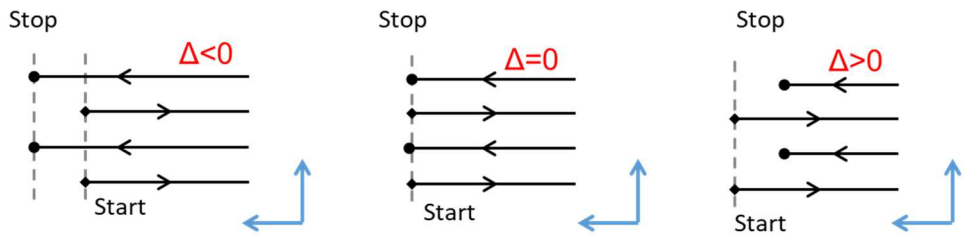

Fig. 22. Schematic representation of the change in delta depending on the stop position relative to start

Table 8.
Delta parameters

Parameters	Values (µm)

Delta negative, Δ < 0 (µm)	−140, −120, −100, −80, −60, −40, −20
Delta equal to zero, Δ = 0 (µm)	0
Delta positive, Δ > 0 (µm)	20, 40, 60, 80, 100, 120, 140

Fig. 23 shows the side surface roughness as a function of Δ. The standard compensation value recommended by the LPBF machine manufacturer was Δ = −20 µm. The areal average roughness in this case was approximately 23 µm, corresponding to the value obtained during the VED optimization discussed in Section 3.1. The graph clearly shows that, when Δ is increased, *Sa* decreases linearly. When Δ is −140 µm, *Sa* equals 50 µm, whereas, when Δ = 140 µm, *Sa* equals 11 µm. Therefore, the roughness can be decreased by a factor of five by changing the Δ compensation.

To better understand these results, an SEM analysis was performed on three different samples of the batch: i) Δ = −140 µm, ii) 0 µm, and iii) 140 µm. The side surfaces and edges of the top surfaces were observed and revealed highly different topographies. For negative or null Δ, an important amount of balling and attached particles can be observed. Furthermore, the scan strategy is visible because the distance between the scan vectors (hatch distances) can be observed. Positive delta scan vectors are not visible, and less balling and fewer attached particles can be observed.

The reason for this can be explained first at the weld track level (see Fig. 24).

- The front head of the end vectors generates a melt pool (and a solidified boundary) with a very coarse radius. Consequently, the end vectors generate coarse surfaces. Furthermore, the large melt pool on the end absorbs more powder in a short time owing to the high temperature. This leads to an increase in the amount of liquid. The liquid penetrates the surrounding powder but cannot melt it sufficiently. As a result, balls are formed from partially molten and solidified material.
- In the opposite start, the vectors generate finer surfaces at their back head. The radius of the melt pool was smaller, and only a small number of powder particles were attached to the surface.

Therefore, most of these observations are in agreement with the melt pool hydrodynamics (comet shape) [30, 35].

At the workpiece level, adjusting the Δ compensation makes it possible to hide or emphasize the presence of coarse surfaces generated by the front head of the end vectors.

- A negative compensation value highlights surfaces generated by the front head of the end vectors (coarse radius, balling, and unfused particles). As a consequence, rough surfaces are obtained.
- A positive compensation value hides the surfaces generated by the front head of the end vectors. Consequently, finer surfaces are obtained (finer radius, less balling, and unfused particles).

Finally, positive compensation generates a second beneficial effect (see Fig. 25). At high positive compensations, end vectors “sink” into the material and reveal n + 1 layers that are parallel to the generated surface. Vectors parallel to the surface generate finer surfaces. However, a detrimental effect of such compensation is that the sample dimensions are governed by the parallel vectors. Perpendicular vectors should rule the sample dimensions.
At higher positive compensations, no further beneficial effect is observed because the n + 1 layer then rules the topography. Moreover, porosity is likely to appear.

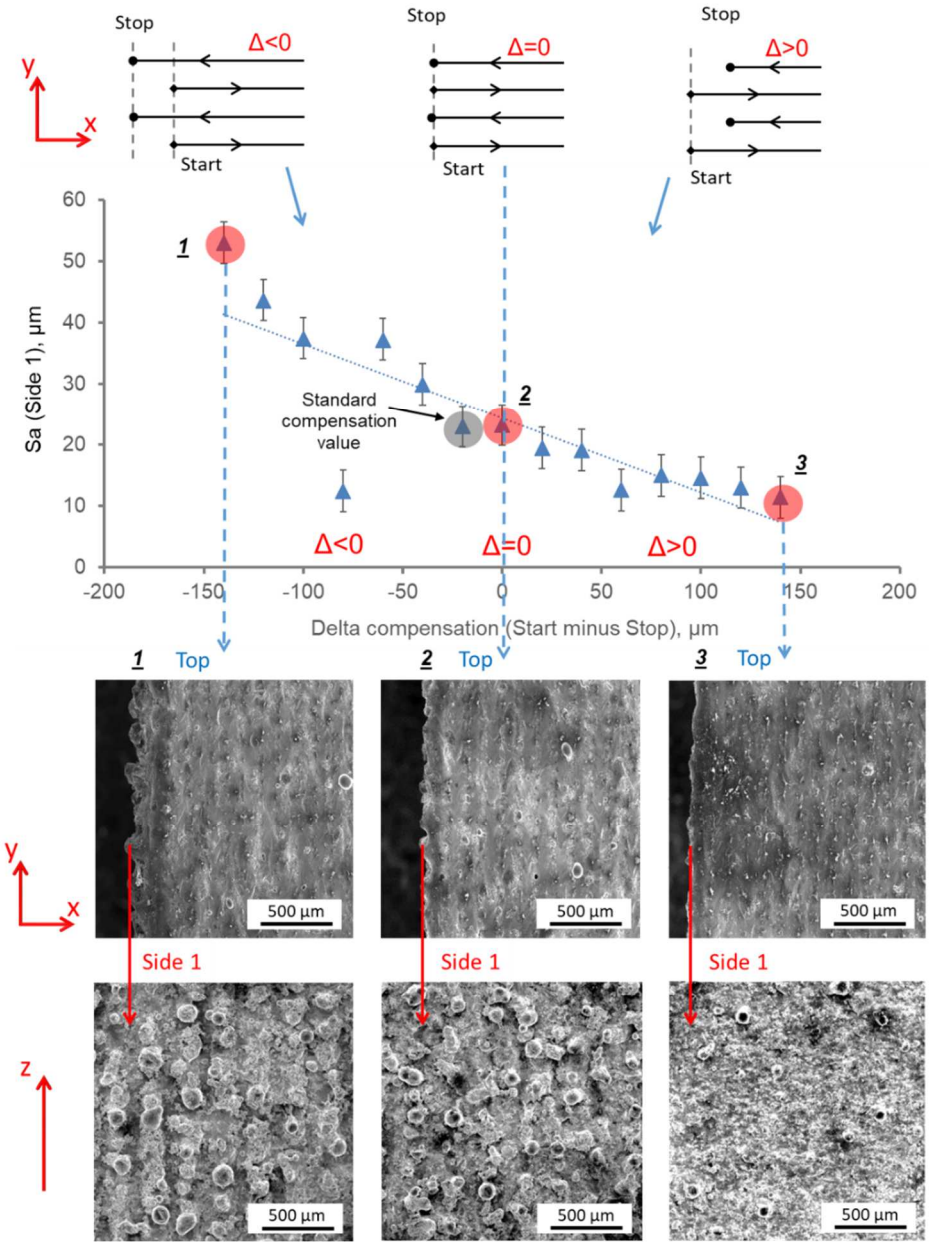

Fig. 23. Side surface roughness decreases from 50 to 11 µm in the Δ positive direction

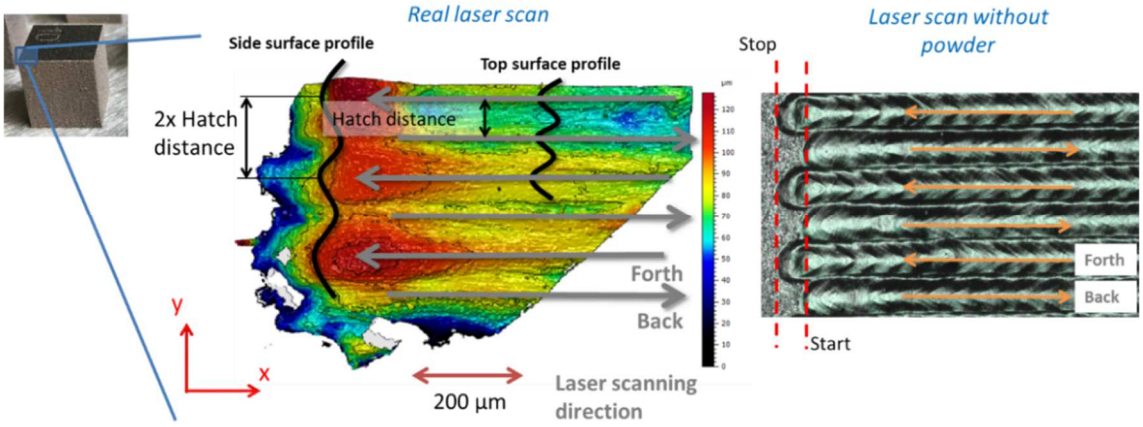

Fig. 24. Shape of the solidified melt pool at the end and beginning of the weld track with [21] and without powder

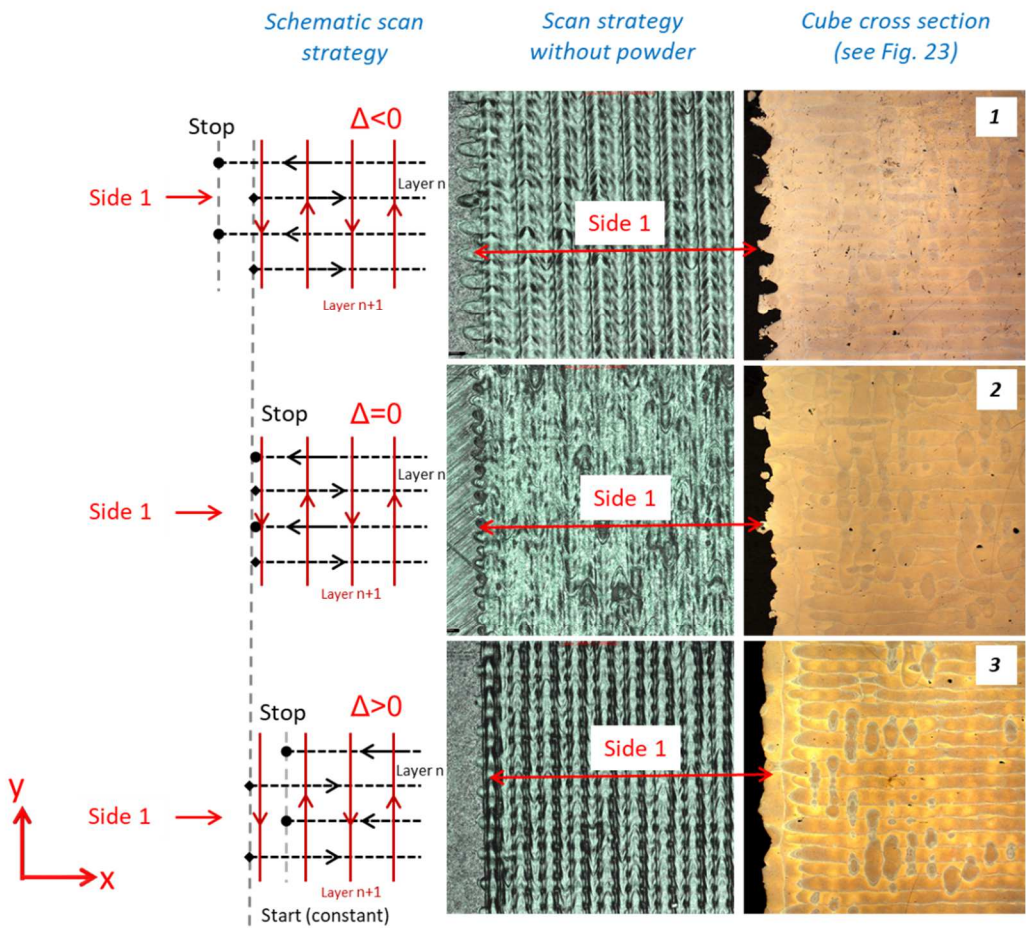

Fig. 25. End of the weld tracks disappearing inside the cube for the benefit of layer n + 1 tracks, parallel to the generated surface

3.3.2. Contour settings

A classic way to improve AM surfaces is to generate samples with weld tracks parallel to the side surfaces [17, 18]. This is known as "contouring." However some disadvantages of this method are reported in several references:

- Potential different metallurgical behaviors between the heart and the contour [47]
- Potential porosities between the heart and the contour [43, 44]
- Contour scanning is detrimental for slightly inclined surfaces ($\alpha < 30^{o}$) [36, 40]

For these reasons, contour settings were not considered as the only solution to improve the roughness in this study.

Two contour settings were studied and are presented in Fig. 26.

- In the first case, the internal area of the sample (heart) is first filled in (with the classical back and forth strategy), and the contour scan is performed afterward. This setting is called "Scan then contour".
- In the second case, a contour is first performed, and then the inner area (heart) of the sample is filled in (with the classical back and forth strategy). This setting is called "Contour then scan."

The same optimized primary process parameters were used for contour scanning. Fig. 27 shows the effect of the contour settings on the surface roughness. Considering a cube with basic parameters and without contour settings, the roughness value remains within the limit of 20 µm. However, when a contour is added, the surface roughness changes as follows.

- Contour setting "Scan then contour" increases the roughness by 6.5%.
- Contour setting "Contour then scan" reduces the roughness by 57.4% (decrease of areal average roughness from 22.7 to 10.3 µm).

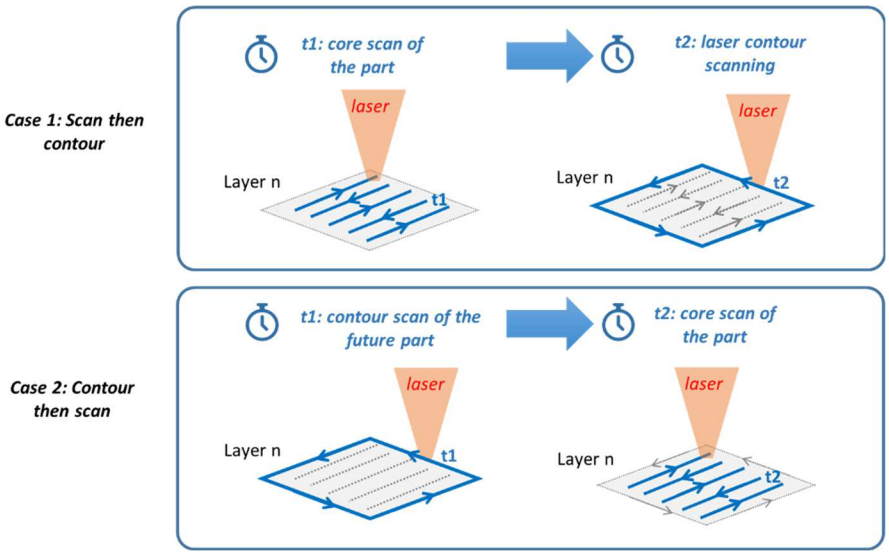

Fig. 26. Two cases of contour settings: “Scan then contour” and “Contour then scan”

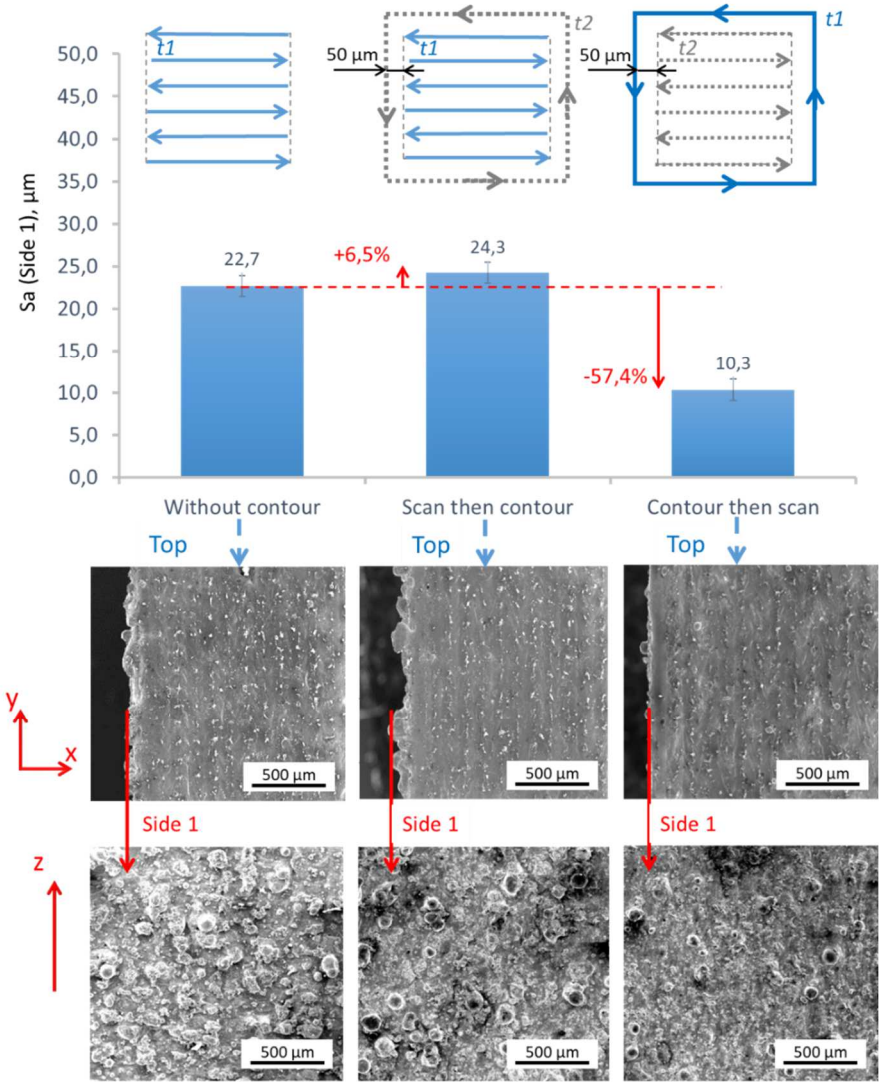

Fig. 27. The effect of the contour on the side surface roughness

An explanation for the better roughness obtained if the contour is performed before the normal scan is as follows.

- In the case of "Contour then scan," the contour path crosses a homogeneous powder bed (see Fig. 28).
- In the case of "Scan then contour," the contour path crosses a powder bed that can be modified by the first scan paths. As a consequence, the powder bed is less regular, and balling effects can appear. The contour plays the role of remelting partly in the first scan, but surface roughness can even deteriorate because it scans a heterogeneous powder bed (see Fig. 29).

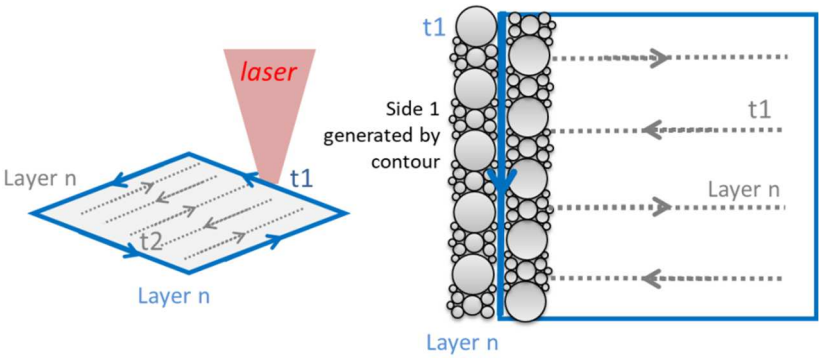

Fig. 28. Contour setting "Contour then scan"

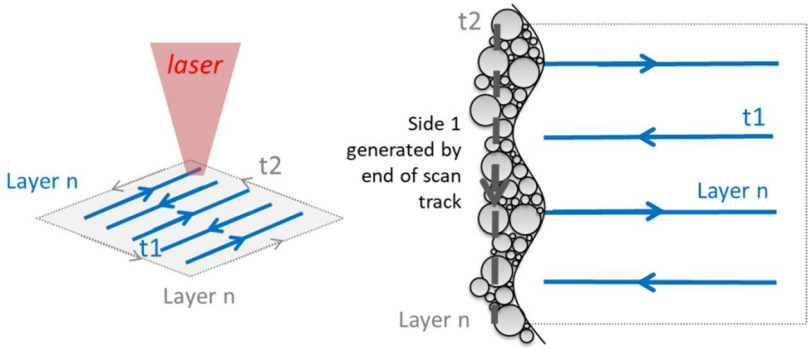

Fig. 29. Contour setting "Scan then contour"

4. Conclusions

LPBF side surface generation was studied for optimization purposes. The material of interest was AlSi10Mg. To understand the surface generation better, the work was divided into three main sequences: i) a study on primary process parameters was performed to find the first surface and density optimum, ii) surface roughness dispersion was studied, and iii) a study on the influence of secondary parameters on surface roughness was conducted.

The following conclusions can be drawn for each sequence.

- Primary parameter optimization
  - The porosity, top, and side surface roughness (*Sa*) followed similar trends as a function of the VED.
  - Consequently, an optimal window capable of minimizing both surface roughness and porosity can be found. The optimal VED was found to be between 60 and 85 J/mm^3. This optimal window is applicable for an AlSi10Mg powder with a size distribution of 5–25 µm. A powder with a smaller particle size would require a higher VED.
  - Based on this first optimization, the *Sa* value could be reduced from 40 to 20 µm.
- Surface roughness dispersion study
  - The roughness variations from one plate to the other can be rather low but greatly depends on the location on the plate: higher in the corners of the plates (variation up to 7 µm) and much lower in the middle of the plates (variation of 1 µm).
  - Differences in areal average roughness from one side to the other are significant and can reach as much as 9 µm ($\sigma = 4.9$ µm). This is because the sample size is not a multiple of the hatch distance, leading to different weld track configurations on each side.

- Finally, roughness dispersions on the same side of a sample are rather low (approximately 2 µm, $\sigma = 1.25$ µm).
- Based on these observations, it is recommended at least to measure the center part of the side to obtain a representative average roughness. It is important to measure the same sample side for comparison purposes and be aware of the important dispersion from one side to another. The rather high roughness values obtained in this study can be partially explained by the choice of a "rough" side.

- Secondary parameter influence on surface roughness
  - Two parameters/options are important to reduce roughness: compensation and contour. By observing the influence of these parameters, a better understanding of the surface generation in the LPBF process can be achieved.
    - The front head of the weld track forms irregularities when it reaches the sample side. This is because of the large radius and high temperature of the melt pool at the end of the weld track, which absorbs large amounts of powder. In the opposite case, the vectors generate finer surfaces at their back head.
    - Adjusting the compensation (positioning of start and end vectors) hides surfaces generated by the front head of the end vectors to benefit the surfaces generated by the back head of the start vectors. This induces the generation of finer surfaces (down to an *Sa* of 10 µm)
    - A classic way to improve AM surfaces is to generate samples with weld tracks parallel to the side surfaces. This is known as "contouring." If the contour is performed before scanning the heart of the sample, the laser crosses a homogeneous powder bed, leading to a fine surface roughness (*Sa* of 10 µm). If the contouring is performed after scanning the heart of the sample, the laser crosses an inhomogeneous powder bed, leading to a rougher surface (*Sa* of 25 µm).

Based on the different findings, it was possible to decrease the roughness significantly from an *Sa* of 40 µm to an *Sa* of 10 µm.

5. Prospects

- **The need for more advanced surface characterization:** in the future, observation of other surface roughness parameters as proposed in [21] and the use of specific analysis (PSD, fractal analysis) could increase the understanding of topography generation.
- **Surface roughness and complex parts:** Regarding the different findings, geometrical positioning of the different weld tracks is an important issue to address in order to reduce surface roughness. Knowing that the parts produced by LPBF are designed to be complex, important questions must be addressed.
  - How can roughness be homogenized from one side to the other (without postprocessing surfaces)?
  - Contour is interesting for vertical side surfaces, but its interest is limited for inclined surfaces owing to the staircase effect. Can better positioning of weld tracks help reduce the roughness of inclined samples?
  - More complex strategies (for example to reduce residual stresses) should be studied and compared to the results of this article.

Acknowledgments

The authors wish to thank DGE, BPI, Région Auvergne-Rhône-Alpes, and Saint-Etienne Métropole for the financial support of the 3D Hybride FUI project. Furthermore, the authors wish to thank the project partners (GIE Manutech USD, Lifco, Ireis, WeAre Tech, Safran, Ecole des Mines de Saint-Etienne, ENISE, and Jean Monnet University) for their contributions in person-hours. Finally, they are grateful to Elodie Cabrol and Maryane Jacquier from Centrale Lyon – ENISE and LTDS for their help in powder characterization and porosity analysis.

References

[1] Aeronautical materials for today and tomorrow, Following the forum organized by the Air and Space Academy (AAE), French Aerospace Society (3AF) and Academy of Technologies, (2012)

[2] A. Leon, E. Aghion, Effect of surface roughness on corrosion fatigue performance of AlSi10Mg alloy produced by Selective Laser Melting (SLM), Materials Characterizataion 131 (2017) 188–194.

[3] I. M. Kusoglu, B. Gökce, S. Barcikowski, Research trends in laser powder bed fusion of Al alloys within the last decade, Additive Manufacturing 36 (2020) 1014892

[4] A. du Plessis, S. Beretta, Killer notches: The effect of as-built surface roughness on fatigue failure in AlSi10Mg produced by laser powder bed fusion, Additive Manufacturing 35 (2020) 101424

[5] O. Poncelet, M. Marteleur, C. van der Rest, O. Rigo, J.Adrien, S. Dancette, P. J. Jacques, A. Simar, Critical assessment of the impact of process parameters on vertical roughness and hardness of thin walls of AlSi10Mg processed by laser powder bed fusion, Additive Manufacturing (2020) doi:https://doi.org/10.1016/j.addma.2020.101801.

[6] L. Wang, S. Wang, J. Wu, Experimental investigation on densification behavior and surface roughness of AlSi10Mg powders produced by selective laser melting, Optics and Laser Technology 96 (2017) 88–96.

[7] R. Liu, Z. Wang, T. Sparks, F. Liou, J. Newkirk, Aerospace applications of laser additive manufacturing, In: Laser additive manufacturing, Woodhead Publishing (2017) 351-371.

[8] W. Pei, W. Zhengying, Ch. Zhen, D. Jun, H. Yuyang, L. Junfeng, Z. Yatong, The AlSi10Mg samples produced by selective laser melting: single track, densification, microstructure and mechanical behavior, Applied Surface Science 408 (2017) 38-50.

[9] S. A.M. Tofail, E. P.Koumoulos, A. Bandyopadhyay, S. Bose, L. O'Donoghue, C. Charitidis, Additive manufacturing: scientific and technological challenges, market uptake and opportunities, Materials today 21 (2018) 22-37.

[10] D. Herzog, V. Seyda, E. Wycisk, C. Emmelmann, Additive manufacturing of metals, Acta Materialia 117 (2016) 371–392.

[11] M. H. Nasab, D. Gastaldi, N. F. Lecis, M. Vedani, On morphological surface features of the parts printed by selective laser melting (SLM), Additive Manufacturing 24 (2018) 373–377.

[12] B. Liu, R. Wildman, C. Tuck, I. Ashcroft, R. Hague, Investigation the effect of particle size distribution on processing parameters optimization in selective laser melting process, Additive Manufacturing Research Group, Loughborough University (2011) 227-238.

[13] A. Townsend, N. Senin, L. Blunt, R.K. Leach, J.S. Taylor, Surface texture metrology for metal additive manufacturing: a review, Manufacturing Metrology Team, Precision Engineering 46 (2016) 34–47.

[14] K. Kempen, L. Thijs, J. V. Humbeeck and J.P. Kruth, Processing AlSi10Mg by selective laser melting: parameter optimisation and material characterization, Materials Science and Technology 31 (2015) 918-923.

[15] C. K. Stimpson, J. C. Snyder and K. A. Thole, Roughness effects on flow and heat transfer for Additively manufactured channels, Journal of Turbomachinery (2015) 138 (5).

[16] A. P. Nagalingam, S.H.Yeo, Surface finishing of additively manufactured Inconel 625 complex internal channels: A case study using a multi-jet hydrodynamic approach, Additive Manufacturing 36 (2020) 101428.

[17] F. Calignano, D. Manfredi, E. P. Ambrosio, L. Iuliano, P. Fino, Influence of process parameters on surface roughness of aluminum parts produced by DMLS, The International Journal of Advanced Manufacturing Technology 67 (2013) 2743–2751.

[18] Y. Tian, D. Tomus, P. Rometsch, X. Wu, Influences of processing parameters on surface roughness of Hastelloy X produced by selective laser melting, Additive Manufacturing 13 (2017) 103-112.

[19] B. Zhang, Y. Li, Q. Bai, Defect Formation Mechanisms in Selective Laser Melting: A Review, Chin. J. Mech. Eng. 30 (2017) 515–527.

[20] M. Attaran, The rise of 3-D printing: The advantages of additive manufacturing over traditional manufacturing, Business Horizons 60 (2017) 677-688.

[21] F. Cabanettes, A. Joubert, G. Chardon, V. Dumas, J. Rech, C. Grosjean, Z. Dimkovski, Topography of as built surfaces generated in metal additive manufacturing: A multi scale analysis from form to roughness, Precision Engineering 52 (2018) 249-265.

[22] C. Y. Yap, C. K. Chua, Z. L. Dong, Z. H. Liu, D. Q. Zhang, L. E. Loh and S. L. Sing, Review of selective laser melting: Materials and applications, Applied physics reviews 2, 041101 (2015).

[23] D. Gu, Y. Shen, Balling phenomena during direct laser sintering of multi-component Cu-based metal powder, Journal of Alloys and Compounds 432 (2007) 163–166.

[24] R. Li, J. Liu, Y. Shi, L. Wang, W. Jiang, Balling behavior of stainless steel and nickel powder during selective laser melting process, The International Journal of Advanced Manufacturing Technology 59 (2012) 1025–1035.

[25] K. Mumtaz and N. Hopkinson, Top surface and side roughness of Inconel 625 parts processed using selective laser melting, Rapid Prototyping Journal 15 (2009) 96-103.

[26] A. Boschetto, L. Bottint, F. Veniali, Roughness modeling of AlSi10Mg parts fabricated by selective laser melting, Journal of materials processing technology 241 (2017) 154-163.

[27] F. Trevisan, F. Calignano, M. Lorusso, J. Pakkanen, A. Aversa, E. P. Ambrosio, M. Lombardi, P. Fino and D. Manfredi, On the Selective Laser Melting (SLM) of the AlSi10Mg Alloy: Process, Microstructure and Mechanical Properties, Materials 10 (2017) 1-23.

[28] T.B. Sercombe and X. Li, Selective laser melting of aluminium and aluminium metal matrix composites: review, Materials Technology 31 (2016) 77-85.

[29] Y. Yang J. Lu, Z. Luo, Di Wang, Accuracy and density optimization in directly fabricating customized orthodontic production by selective laser melting, Rapid Prototyping Journal 18 (2012) 482 – 489.
[30] T. Yang, T. Liu, W. Liao, E. MacDonald, H. Wei, X. Chen, L. Jiang, The influence of process parameters on vertical surface roughness of the AlSi10Mg parts fabricated by selective laser melting, Journal of Materials Processing Tech. 266 (2019) 26-36.
[31] M. Mohammadi, H. Asgari, Achieving low surface roughness AlSi10Mg 200C parts using direct metal laser sintering, Additive Manufacturing 20 (2018) 23–32.
[32] E. Yasa, J. Kruth, Application of laser re-melting on Selective Laser Melting parts, Advances in Production engineering & Management 6 (2011) 4, 259-270.
[33] Y. Liu, J. Zhang, Y. Yang, J. Li, J. Chen, Study on the influence of process parameters on the clearance feature in non-assembly mechanism manufactured by selective laser melting, Journal of Manufacturing Processes 27 (2017) 98–107.
[34] K. Kamarudin, M.S. Wahab, Z. Shayfull, A. Ahmed, and A.A. Raus, Dimensional Accuracy and Surface Roughness Analysis for AlSi10Mg Produced by Selective Laser Melting (SLM), MATEC Web of Conferences **7**8 (2016) 01077.
[35] B. Li, Z. Li, P. Bai, B. Liu and Z. Kuai, Research on Surface Roughness of AlSi10Mg Parts Fabricated by Laser Powder Bed Fusion, Metals 8(7):524 (2018).
[36] D. Bhaduri, P. Penchev, S. Dimov, K. Essa, L. N. Carter, C. I. Pruncu, J. Jiang, D. Pullini, On the surface integrity of additive manufactured and post-processed AlSi10Mg parts, Procedia CIRP 87 (2020) 339-344.
[37] A. H. Maamoun, J. Xue , M. A. Elbestawi and S. C. Veldhuis, Effect of Selective Laser Melting Process Parameters on the Quality of Al Alloy Parts: Powder Characterization, Density, Surface Roughness and Dimensional Accuracy, Materials 11 (2018) 2343.
[38] D. Wang, Y. Liu and Y. Yang, Theoretical and experimental study on surface roughness of 316L stainless steel metal parts obtained through selective laser melting, Rapid Prototyping Journal 22 (2016) 706 – 716.
[39] O. Poncelet, M. Marteleur, C. van der Rest, O. Rigo, J. Adrien, S. Dancette, P.J. Jacques and A. Simar, Critical assessment of the impact of process parameters on vertical roughness and hardness of thin walls of AlSi10Mg processed by laser powder bed fusion, Additive Manufacturing, (2020) doi:https://doi.org/10.1016/j.addma.2020.101801.
[40] Jitka Metelkova, Lars Vanmunster, Han Haitjema and Brecht Van Hooreweder, Texture of inclined up-facing surfaces in laser powder bed fusion of metals, Additive Manufacturing, (2020) doi:https://doi.org/10.1016/j.addma.2021.101970.
[41] M. A. Balbaa, et al, Role of powder particle size on laser powder bed fusion processability of AlSi10mg alloy, Additive Manufacturing 37 (2021): 101630.
[42] Jun Hao Tan, Wai Leong Eugene Wong and Kenneth William Dalgarno, An overview of powder granulometry on feedstock and part performance in the selective laser melting process, Additive Manufacturing 18 (2017): 228-255.
[43] T. Reiber, J. Rüdesheim, M. Weigold, E. Abele, J. Musekamp, M. Oechsner, Influence of contour scans on surface roughness and pore formation using Scalmalloy® manufactured by laser powder bed fusion (PBF-LB), Materialwissenschaft und Werkstofftechnik 52.4 (2021): 468-481.
[44] P. Karimi, C. Schnur, E. Sadeghi, J. Andersson, Contour design to improve topographical and microstructural characteristics of Alloy 718 manufactured by electron beam-powder bed fusion technique, Additive Manufacturing 32 (2020): 101014.
[45] Xingchen Yan et al., Effect of building directions on the surface roughness, microstructure, and tribological properties of selective laser melted Inconel 625, Journal of Materials Processing Technology 288 (2021): 116878.
[46] G. Strano, L. Hao, R. M. Everson, K. E. Evans, Surface roughness analysis, modelling and prediction in selective laser melting, Journal of Materials Processing Technology 213.4 (2013): 589-597.
[47] D. Mallipeddi, et al., Surface Integrity of Machined Electron Beam Melted Ti6Al4V Alloy Manufactured with Different Contour Settings and Heat Treatment, Procedia CIRP 87 (2020): 327-332.